RSC Advances

PAPER

View Article Online
View Journal | View Issue

Cite this: *RSC Adv.*, 2026, **16**, 12759

Propagation of THz magnons in a one-dimensional transition metal decorated holey graphyne strip with tunable bandgaps

Prabin Pyakurel Sharma, Chaithanya Purushottam Bhat and Debashis Bandyopadhyay *

We report *ab initio* and model-Hamiltonian investigations of THz magnon propagation in a transition metal adatom decorated one-dimensional nanoscale strip derived from a holey graphyne (HGY) sheet. Using density functional theory (DFT) for the *ab initio* study of the system and then applying a tight binding model through Wannier functions, we obtain localized magnetic moments that can be studied using the Heisenberg spin model and linear spin wave theory. Our results show magnon propagation in the material with velocities reaching up to 5.5 km s^{-1} along with bandgaps that can be tuned by up to 10% using an external magnetic field. These findings suggest that transition metal decorated one-dimensional HGY nanostrips act as atomically thin magnonic crystals with field tunable transmission bands, making them promising platforms for next-generation magnonic and wave-based computing devices operating in the terahertz range. Experimental realization through bottom–up synthesis, combined with spin wave spectroscopy or scattering measurements, could open new opportunities for exploring ultrafast spin dynamics in these materials.

Received 13th December 2025
Accepted 22nd February 2026

DOI: 10.1039/d5ra09647b

rsc.li/rsc-advances

1. Introduction

The transfer of angular momentum in the form of spin waves can be used to transmit information without transferring electronic charge. The quanta of these spin waves are bosonic quasiparticles called magnons, which form the basis for magnonics. Utilizing magnons for data transfer eliminates the ohmic losses associated with electrons, which in turn facilitates greater miniaturization and more energy-efficient devices.[1–4] Furthermore, the versatility of magnons opens up a frequency range from GHz to THz, as well as the possibility for novel wave-based computing.[5] A primary objective is to achieve the directed propagation of magnons, where their speed, direction, and propagating frequencies can be precisely tuned.

The propagation of magnons depends primarily on crystal structure and material composition, which may be dynamically tuned by temperature gradients, strain, or external magnetic fields. Significant research efforts have combined these degrees of freedom to achieve desired properties. Propagation velocity and frequency have been manipulated using temperature gradients, external magnetic fields, strain, or topological properties.[6–12] However, the focus has predominantly been on GHz magnonics using yttrium iron garnet (YIG) or permalloy, which are unlikely to fulfill the requirements of miniature, high-frequency, ultrafast spin wave guides.[4,13–15] This motivates the search for alternative templates over which high-frequency spin waves can propagate. The emergence of altermagnetism in monolayers like $VPSe_3$ offers new avenues for spin splitting and valley control *via* electric fields and Janus structures.[16] Simultaneously, the study of ultrafast, terahertz spin waves is expected to bridge the scientific gap in our understanding of the THz frequency range as they lie between the electronic and photonic regimes.[17,18]

THz spin waves offer the potential for ultrafast signal processing, denser integration due to shorter wavelengths, and direct compatibility with emerging THz communication technologies.[17,18] This can be achieved when spin wave propagation is dominated by exchange interactions, which lie at a higher energy level than other magnetic interactions.[19,20] Recent investigations into $FePS_3$ and $NiPS_3$ monolayers have utilized first-principles calculations and machine learning to establish exact spin Hamiltonians, revealing how competing exchange interactions and anisotropy define their unique spin-wave spectra.[21] Exchange interactions dominate over dipolar and other long-range interactions as the size of a magnetic material decreases. Hence, ultrathin nanostructures have been identified as ideal candidates for tuning exchange spin waves.[22] Theoretical and experimental works exploring atomically thin films for exchange-dominated spin wave propagation[23–25] show promising results through material nanostructuring. In particular, magnonic waveguides confined in one dimension are more efficient, as cross-propagating waves are absent due to the geometry.

Department of Physics, Birla Institute of Technology and Science Pilani, Rajasthan 333031, India. E-mail: bandy@pilani.bits-pilani.ac.in

A requirement for the directed propagation of select THz frequencies is the availability and tunability of bandgaps, which allow for the selection of transmitted frequencies, noise avoidance, and the filtering of unwanted signals.[26] Bandgaps in a magnonic crystal arise when the Bragg resonance condition is fulfilled, leading to destructive interference and the creation of a "forbidden zone" in energy where no spin waves can propagate.[27] As such, the simplest way to tailor them is by controlling periodicity in a waveguide or using line defects.[28] Other proposed methods to engineer the magnonic bandgap include altering geometric parameters or coupling two magnonic crystals.[28,29] Bandgaps can also be dynamically tuned during operation using temperature gradients, pressure, or magnetic fields.[8,29–31] Specifically, an external magnetic field introduces a Zeeman term in the spin Hamiltonian, predictably shifting the magnonic dispersion and allowing for straightforward tuning of the bandgap position. A THz frequency waveguide combined with dynamically tunable bandgaps would be of enormous utility in computing systems.

One-dimensional (1D) magnonic crystals are especially relevant for confining and filtering spin wave modes and for the nanoscale control of dispersion.[28,32] The widths and center frequencies of magnonic bandgaps in 1D crystals can be finely adjusted by varying component materials, stripe width, and magnetic field orientation.[33] Such crystals have been created *via* width modulation, spatial patterning, or microcavity creation to produce sharp frequency peaks and well-defined bandgaps.[4,9,34,35] The discovery of ferromagnetism in single-layer van der Waals materials has highlighted how nanoscale systems can support ultrafast THz magnons.[22,36–39] Moreover, materials such as $OsBr_2$ monolayers demonstrate the coexistence of magnetic, ferroelectric, and ferrovalley orders, which can be dynamically manipulated through phase transitions or interlayer sliding.[40] While the Mermin–Wagner theorem states that long-range magnetic order cannot exist in an infinite 1D or 2D system, Jenkins *et al.*[41] found that finite-sized materials (up to several micrometers) can still maintain magnetic ordering. Therefore, it is prudent to nanostructure 1D ultrathin materials to host directed THz spin waves.

The abundance of low-dimensional, carbon-based materials is well-suited for this purpose due to carbon's versatile chemistry, which allows for precise geometric engineering *via* nanofabrication.[42] The addition of dopants and functionalization of carbon allotropes has yielded stable materials with useful properties for energy storage, catalysis, or magnetism.[43–45] First principles calculations indicate that transition metal (TM) atoms chemisorb strongly on graphyne-like sheets, particularly at acetylenic bridges, resulting in magnetic moments.[32] Furthermore, TM-doped graphyne nanoribbons are predicted to exhibit ferromagnetism and even half-metallicity; for instance, Mn- or Co-doped graphyne ribbons show 100% spin polarization at the Fermi level.[46]

A stable 1D allotrope of carbon with periodic magnetic patterning is therefore expected to function as a THz-range, band-tunable magnonic crystal. The recent synthesis of holey graphyne (HGY) by Liu *et al.*[47] provides such an opportunity. HGY is a porous 2D carbon allotrope composed of alternating benzene rings and diacetylenic linkers, featuring uniformly distributed sp and sp^2-hybridized carbons.[48] Interest in this material is growing for energy storage, topological states, and magnonic applications.[16,45,49] First principles calculations by Bhat *et al.* indicate that TM atoms form stable systems with HGY through Dewar interactions.[45]

In this study, we propose a transition metal decorated holey graphyne strip as a novel 1D magnonic crystal capable of hosting ultrafast THz-range spin waves and field tunable bandgaps. The strip structure follows the precursor to the HGY sheet during synthesis, suggesting the feasibility of synthesizing a 1D material strip. We explore the available frequency bands and dynamic characteristics, such as propagation velocity, using linear spin wave theory (LSWT). Furthermore, the effect of the magnetic field on the bandgap is examined. Our results indicate that these HGY strips exhibit appropriate magnetic interactions and the potential for high-frequency magnon propagation, making them promising candidates for magnonic applications.

2. Methodology

We first design the holey graphyne (HGY) strip by confining it in two dimensions and verify its stability using *ab initio* molecular dynamics (AIMD). We employ density functional theory (DFT) to investigate the electronic structure of these strips functionalized with transition metal (TM) adatoms (V, Cr, Mn, Fe, Co, and Ni). To determine the localized contributions to magnetism, we construct maximally localized Wannier functions (MLWFs).[50] The exchange interactions are then extracted using the Tight Binding to Exchange (TB2J) method,[51] and the magnon dispersion relations are calculated using linear spin wave theory (LSWT).[52]

The electronic structure and geometry of the HGY strip with magnetic adatoms were calculated using spin-polarized DFT as employed in the Vienna *Ab Initio* Simulation Package (VASP) with the Perdew–Burke–Ernzerhof (PBE) GGA functional.[53–55] To account for on-site correlation effects, we employed the DFT+U approach with $U = 2$ eV for Fe/Co/Mn, $U = 1$ eV for V, and $U = 0$ for Ni.[56] We used a unit cell of 40 carbon atoms and introduced 11 Å of vacuum on either side of the strip to avoid interactions between periodic images. A $1 \times 4 \times 1$ Monkhorst–Pack k-point grid was used to sample the Brillouin zone. The convergence criteria were set to 0.005 eV $Å^{-1}$ for the relaxation of Hellmann–Feynman forces and 10^{-5} eV for total energy. A kinetic energy cutoff of 520 eV was used for plane-wave expansion. AIMD simulations were performed to check the stability of the strip-adatom system at 300 K using a 5 ps production run with a time step of 0.07 fs. The temperature was maintained using a Nosé–Hoover thermostat.

MLWFs were constructed from the DFT Bloch states using the Wannier90 package.[50] As the bands near the Fermi level showed dominant contributions from the d orbitals of the TM adatoms, the disentanglement window was chosen to encompass these states, ensuring the resulting Wannier functions were primarily projected onto the d-orbital manifold.

To extract the exchange interactions between magnetic atoms, we use Green's functions in the Wannier basis as implemented in the TB2J package:[51]

$$G_{mn,\mathbf{R}\mathbf{R}'}{}^{\sigma}(E) = \langle w_{m\mathbf{R}}{}^{\sigma}|(E - H^{\sigma})^{-1}|w_{n\mathbf{R}'}{}^{\sigma}\rangle \quad (1)$$

where H^{σ} is the Hamiltonian for spin σ, and wmRσ are spin-dependent Wannier functions. The exchange parameter J_{ij} is then obtained *via* the Liechtenstein formula:[57]

$$J_{ij} = \frac{1}{\pi}\int_{-\infty}^{E_F} \mathrm{d}E \mathrm{Im}\left[\mathrm{Tr}\left(\Delta\Sigma_i{}^{\sigma}(E) G_{ij}{}^{\sigma}(E)\right)\right] \quad (2)$$

where $\Delta\sum_i{}^{\alpha}$ represents the exchange splitting at site i. We map these interactions to a Heisenberg model, including a Zeeman term for external magnetic fields:

$$\hat{H} = -\sum_{\langle i,j\rangle} J_{ij}\mathbf{S}_i\cdot\mathbf{S}_j - g\mu_B\sum_i \mathbf{B}\cdot\mathbf{S}_i \quad (3)$$

where g is the Landé g-factor, $\mathbf{B}$ is the applied magnetic field, and $\mathbf{S}_i$, $\mathbf{S}_j$ are the spins at sites i and j, respectively.

The ground state of the magnetic structure is obtained by using a conjugate gradient method to minimize the energy of the spin system defined by eqn (3). Magnon dispersion was obtained by applying LSWT to this Heisenberg spin Hamiltonian. We followed the formalism of Tóth and Lake,[58] which handles arbitrary magnetic structures *via* Holstein–Primakoff transformations and local coordinate rotations, as implemented in the Sunny.jl library.[52] Following the detailed derivation provided in Section 3 of the SI, the resulting non-interacting second-quantized Hamiltonian is:

$$\mathcal{H} = \sum_{\nu\mathbf{k}} \omega_\nu(\mathbf{k}) a_\nu^\dagger(\mathbf{k}) a_\nu(\mathbf{k}) \quad (4)$$

Finally, we calculate the dynamic structure factor $S(\mathbf{q}, \omega)$ with a Gaussian resolution broadening, which provides a direct link between theory and inelastic neutron scattering (INS) experiments. It is defined as the space- and time-Fourier transform of the spin–spin correlation function:

$$S^{\alpha\beta}(\mathbf{q},\omega) = \frac{1}{2\pi N}\sum_{i,j} e^{i\mathbf{q}\cdot(\mathbf{r}_i-\mathbf{r}_j)}\int_{-\infty}^{\infty}\mathrm{d}t e^{i\omega t}\left\langle S_i{}^{\alpha}(0) S_j{}^{\beta}(t)\right\rangle, \quad (5)$$

where $\alpha, \beta \in \{x, y, z\}$ denote spin components, $\mathbf{r}_i$ is the position of spin i, and N is the total number of spins. Under LSWT, the correlations are dominated by single–magnon processes:

$$S^{\alpha\beta}(\mathbf{q},\omega) = \sum_\nu F_\nu{}^{\alpha\beta}(\mathbf{q})\delta(\omega - \omega_\nu(\mathbf{q})), \quad (6)$$

where $\omega_\nu(\mathbf{q})$ is the energy of the magnon in branch ν, and $F_\nu{}^{\alpha\beta}(\mathbf{q})$ is the corresponding spectral weight.

The measured intensity is proportional to the transverse component of the dynamic structure factor:

$$S_\perp(\mathbf{q},\omega) = \sum_{\alpha,\beta}\left(\delta_{\alpha\beta} - \hat{q}_\alpha\hat{q}_\beta\right) S^{\alpha\beta}(\mathbf{q},\omega), \quad (7)$$

where $\hat{\mathbf{q}} = \mathbf{q}/|\mathbf{q}|$. The relative intensities $F_\nu{}^{\alpha\beta}(\mathbf{q})$ contain information about the polarization and eigenvector structure of the magnon modes.

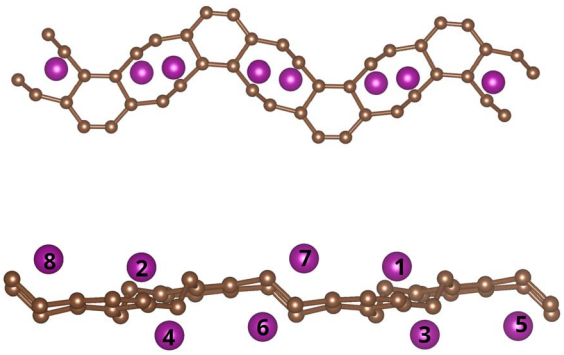

Fig. 1 Representative optimized structure of the TM-decorated holey graphyne strip system, where TM (V, Cr, Mn, Fe, Co, Ni) atoms (purple) and carbon atoms (brown). The numbers label the atoms as used in the text; the upper image is the top view and the lower image is the side view of the optimized structure of the Mn-decorated system.

3. Results and discussion

The ground-state structure of the strip was first optimized using density functional theory (DFT), yielding lattice parameters $a = 20.02$ Å, $b = 20.02$ Å, $c = 21.70$ Å, $\alpha = 90.25°$, $\beta = 85.59°$, $\gamma = 119.99°$. Transition-metal adatoms (TM = V, Cr, Mn, Fe, Co, Ni) were then symmetrically placed above and below the plane at a distance of 2 Å and the structures were re-optimized to obtain their electronic and magnetic properties. Fig. 1 depicts the front and side view of the optimized structure which is representative of the structurally optimized systems. Corresponding optimized structures for all systems are included in the SI (Fig. S1). Thermal stability at ambient conditions was verified *via ab initio* molecular dynamics (AIMD) simulations at 300 K for each structure; as shown in SI (Fig. S2), the total energy remained constant and the temperature, stable throughout the duration of the run. During the AIMD simulation, the carbon-transition-metal bond lengths fluctuate from 2 Å to 2.5 Å for all systems except Ni, which drifts away from the strip (see SI Fig. S3), indicating that the Ni-adatom system, which has weaker interaction with the main strip, is rather unstable at higher temperatures. The reason being that the transition metal is held on to the surface by Dewar interaction. It involves the donation of electrons from carbon atoms and then donation back from the d orbitals of transition metal atoms.[45] The interaction depends on the availability of unpaired d-orbital electrons of transition metal atoms, which increases from vanadium to manganese and then decreases; being nearly filled in Ni.

3.1. Magnetic moments and exchange interactions

From the density of states (DOS) in Fig. 2, the asymmetry in spin-up and spin-down states around the Fermi level is majorly due to the d-orbital of the transition-metal adatom. Therefore, from the electronically optimized wave functions from DFT, we project the d-orbitals of transition-metal adatoms to get the maximally localized Wannier functions. This gave us the magnetic moment localized over each adatom. Table 1 and

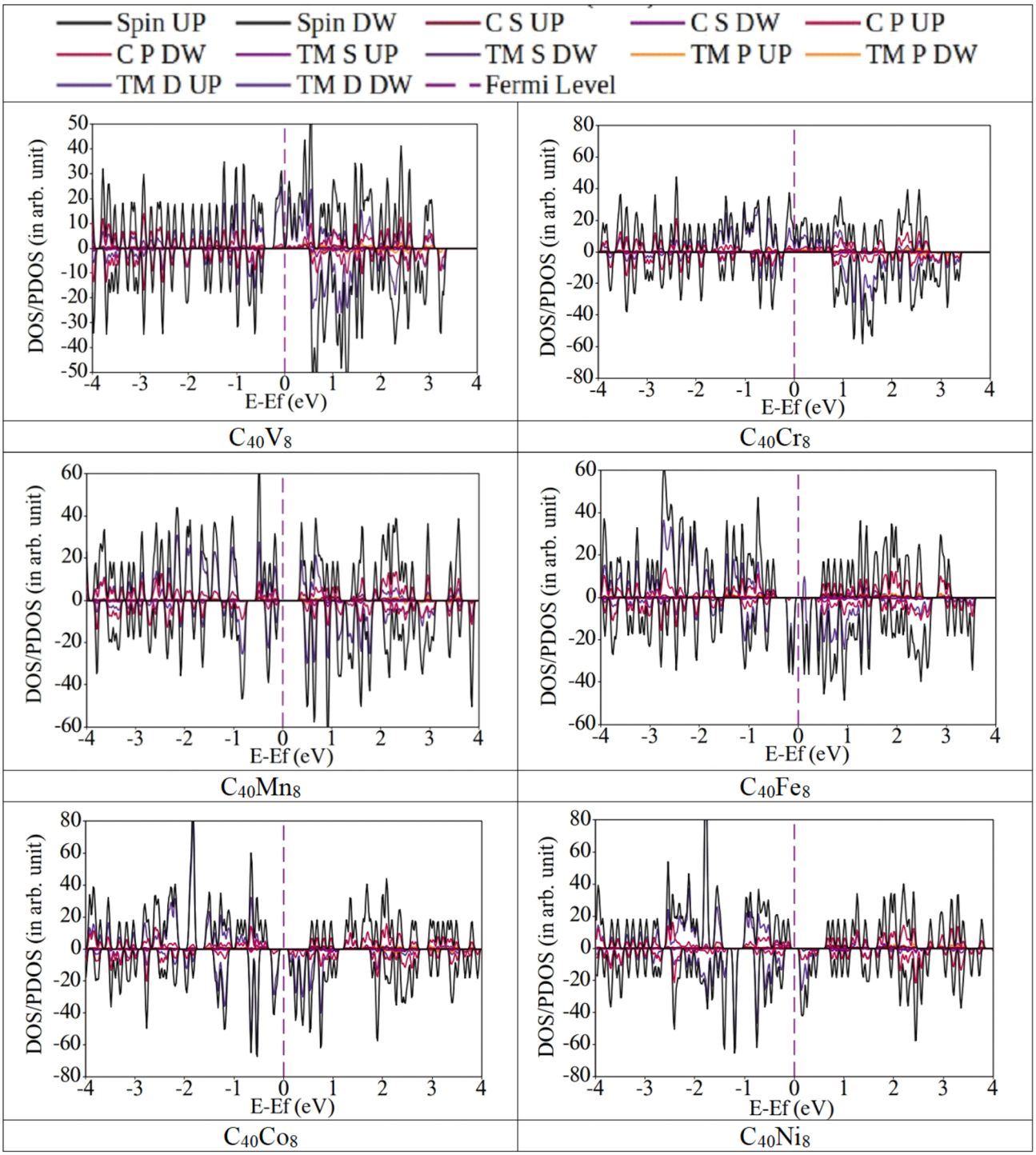

Fig. 2 The density of states for the s, p, and d orbitals obtained from DFT for a holey-graphyne strip with different transition-metal (TM) adatoms: V, Cr, Mn, Fe, Co, and Ni.

Fig. 3 show the magnetic moments on the transition metal atoms over holey graphyne strip. The magnetic moments increase from vanadium to manganese and then start decreasing. This volcano trend is in agreement with previous studies on 3d transition-metal adatoms on γ – graphyne which is a similar system.[32] This is due to the transition metals in the middle of the series having more unpaired electrons while the magnetic moments in either end is quenched giving rise to the volcano plot.

Table 2 shows the nearest neighbor exchange interactions J_{ij} between the transition metal atoms. Since the scale of the strip is in tens of angstroms, dipolar interactions between the magnetic moments are negligible and exchange interaction dominates. A detailed plot of these interactions against distance

Table 1 Magnetic moments (in μ_B) of transition-metal adatoms on the holey graphyne strip

Atom	V	Cr	Mn	Fe	Co	Ni
1	0.17	2.80	3.55	3.88	1.95	0.96
2	0.11	2.06	3.25	3.00	1.95	0.86
3	0.66	1.81	2.46	2.93	2.91	0.97
4	0.73	1.95	3.69	4.13	3.05	1.11
5	0.70	2.84	3.19	1.98	1.95	1.03
6	0.33	2.23	4.49	3.91	3.06	1.15
7	0.48	0.55	1.18	1.21	1.93	0.85
8	0.45	1.80	2.44	2.01	1.94	0.85

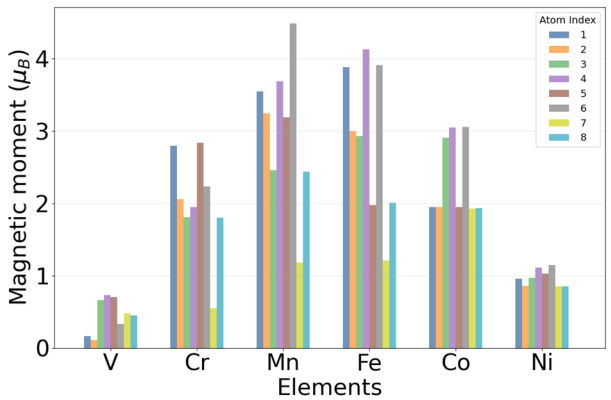

Fig. 3 Magnetic moments of the transition-metal adatoms in holey graphyne strip shows a volcano plot.

is provided in SI Fig. S4 of the SI. All systems have a ferrimagnetic order with strong interactions of ferromagnetic nature and weaker ones of anti-ferromagnetic nature except for Vanadium which is not significantly magnetic. Using the magnetic moments and exchange interactions, we calculated the magnon dispersion relations.

3.2. Magnon spectra of holey-graphyne strip with transition-metal adatoms

3.2.1. Magnon spectrum of $C_{40}Cr_8$ holey-graphyne strip. Fig. 4a shows the magnon bands along the [0, K, 0] directions between the two zone-boundary points (0, −5, 0) and (0, 0.5, 0). The color map shows the normalized scattering intensity obtained from the dynamic structure factor, $S(q, \omega)$. Eight distinct branches appear in the plotted window which are due to the eight distinct Cr moments in the magnetic unit cell. The lowest branch among these are gapless at the zone center identifying it as the acoustic Goldstone magnon. This acoustic branch exhibits a dispersion with bandwidth of 0.13 THz. The nature of the acoustic branch qualitatively follows that of a one-dimensional ferromagnetic spin chain as given by the relation, $E = J \cdot S\ \cos(qa)$,[59] where J is the exchange constant between two spins, S is the spin, a is the lattice constant and q the wavevector. It diverges from the ideal solution as the contributions are from 8 unequal exchange interactions and magnetic moments which are not equidistant to each other.

Right above the acoustic mode, an optical mode of 0.20 THz bandwidth exists separated by 0.47 THz of acoustic-optical bandgap. The mode has a negative curvature relative to the Goldstone mode. At small q, the contribution to scattering intensity from each site cancels off for these optical modes which is seen as vanishing of the color maps near Γ point in Fig. 4. Of the series of optical magnon modes occurring above the first optical mode, the lowest one at 1.05 THz has a bandwidth of 0.10 THz while the rest are nearly dispersionless. These modes are localized intra-unit spin excitations produced by the holey motif and inequivalent Cr environments and do not contribute to propagation.

3.2.2. Magnon spectrum of $C_{40}Mn_8$ holey-graphyne strip. Similar to the $C_{40}Cr_8$, the spin wave dispersion of $C_{40}Mn_8$ (Fig. 4b) has a Goldstone mode but with a much larger bandwidth of 0.95 THz as it has stronger nearest–neighbor exchange interactions as seen in Table 2. There is no bandgap between the first optical mode and acoustic mode as the first optical mode has eigenvectors that are in phase with the acoustic mode which makes their curvatures similar and causes the energy windows of the bands to overlap. The second optical mode however, curves upwards and gives rise to a bandgap between the first and second optical mode of 0.48 THz. It also has a significant bandwidth of 0.47 THz. Unlike the case of Cr, the third optical mode is also quite dispersive with a bandwidth of 0.19 THz. There is also a significant bandgap between the second and third optical mode of 2.7 THz which can act as a good frequency filter. All higher modes are nearly flat as the intra-unit spin interactions take over. Compared with the $C_{40}Cr_8$ strip, the Mn system shows both larger stiffness and higher-energy magnon modes with much larger bandgaps in between. This can be seen as an effect of Mn lying at the middle of the volcano plot in Fig. 3 and having greater values for exchange interactions. It is apparent that Mn-functionalized holey graphyne can host more robust and higher-frequency magnon excitations.

3.2.3. Magnon spectrum of $C_{40}Fe_8$. Although the full energy window between Mn, Fe, Co based systems are numerically similar due to similar magnetic moments; the nature of dispersion relations in Fe-based system (Fig. 4c) shares much in common with the Cr-based system. The acoustic Goldstone mode has a smaller dispersion of 0.34 THz and the curvature of

Table 2 Nearest–neighbor exchange interactions (J_{ij}, in meV) between transition-metal adatoms. The table header lists adatom elements, and the left column specifies atom pairs. Positive J_{ij} values indicate ferromagnetic alignment, and negative values indicate anti-ferromagnetic alignment

Pair(i–j)	V	Cr	Mn	Fe	Co	Ni
1–3	0.00	14.03	6.23	21.22	92.48	17.42
1–7	1.35	5.61	19.22	−1.76	2.97	0.00
2–4	3.72	4.55	12.90	18.61	91.73	17.92
2–8	2.32	9.14	10.08	6.14	2.69	−0.02
3–5	1.54	1.94	11.98	1.61	−3.96	0.28
4–6	4.40	−1.70	13.00	2.33	−0.96	−0.45
5–8	−1.14	−0.40	−11.71	5.35	88.71	41.41
6–7	−0.67	11.42	−7.36	−15.25	91.25	42.33

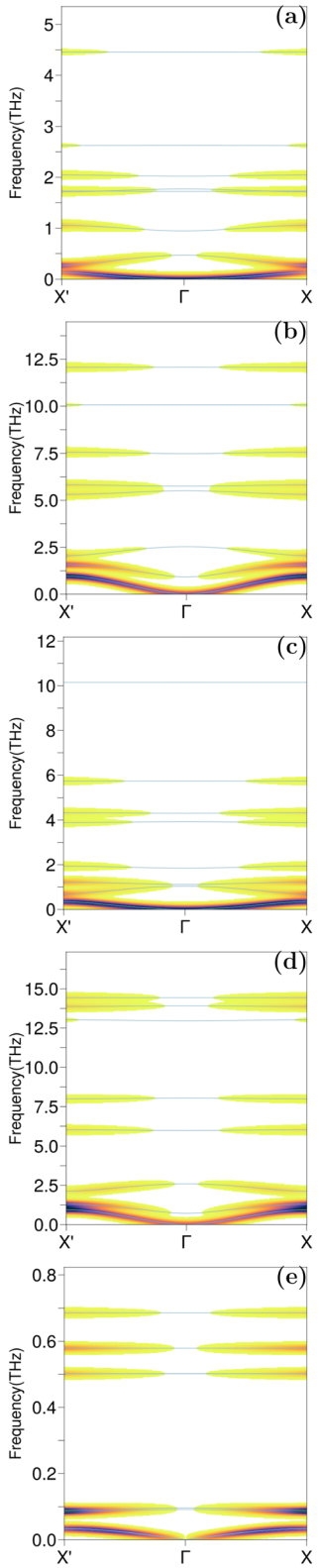

Fig. 4 Calculated magnon bands at 0 K for the $C_{40}TM_8$ (TM = Cr, Mn, Co, Fe, Ni) holey-graphyne strip along (0, *K*, 0) between *X*′(0, −0.5, 0) and *X*(0, 0.5, 0). There are eight branches (one acoustic and seven optical). The color indicates the normalized intensity of inelastic neutron scattering as obtained from the dynamic structure factor. Subfigures: (a) Cr, (b) Mn, (c) Fe, (d) Co, (e) Ni.

the first optical mode is inverted with respect to the acoustic mode. It lies above a bandgap of 0.35 THz from the acoustic mode. Even though the magnetic moments of Fe are similar to Mn, there is a significant antiferromagnetic contribution in the exchange interactions of Fe-based system which decreases the stiffness of the modes. After the first optical mode which has a bandwidth of 0.34 THz, all higher energy modes are mostly dispersionless which results in only the acoustic and first optical mode to contribute to any spin wave propagation separated by an acoustic-optical bandgap.

3.2.4. Magnon spectrum of $C_{40}Co_8$. From Fig. 4d, the magnon dispersion of the Co-based strip exhibits similar features to Mn based strip in that the first mode is a Goldstone mode and the first optical mode shares its nature. This causes it to overlap its energy window with the acoustic mode which stops the acoustic-optical bandgap from forming. It also shares quantitative similarities as the acoustic mode has a bandwidth of 0.94 THz. The first bandgap occurs between the first and second optical modes of 0.84 THz. While the second optical mode is dispersive with bandwidth of 0.46 THz; unlike the Mn-based system the third optical mode is quite flat and has little prospects for spin wave propagation. Even as the spectrum extends up to 15 THz, the Co-based system is much less dispersive than Mn and all the higher optical modes are due to strongly localized magnons.

3.2.5. Magnon spectrum of $C_{40}Ni_8$. The Ni adatoms have the lowest magnetic moments among the five systems studied. The small magnetic moments and exchange interactions in the Ni-based strip leads to all magnon modes existing under 0.7 THz as shown in Fig. 4e. All optical modes are nearly dispersionless and only the acoustic mode has a bandwidth of 0.03 THz. This is a natural consequence of Ni being at the right end of the volcano plot in Fig. 3. Combined with the Ni-adatom being the most unstable among all studied systems, it can be discarded as a candidate for magnonic applications when compared to strips based on other transition metal elements.

The five $C_{40}TM_8$ holey-graphyne strips follow a similar pattern of dispersion relations. The lowest mode is gapless at the *Γ* point which is a characteristic of the Goldstone mode. This mode has a nature similar to the one-dimensional ferromagnetic spin chain. An evolution of the magnon spectra can be seen across the 3d transition-metal series (Fig. 4). The change of the energy scale and magnon dispersion is such that; Ni forms the low-energy limit, Cr is intermediate in energy and dispersion while Co, Mn and Fe produce the largest magnon bandwidths. Cr features a narrow acoustic band, a relatively dispersive first optical mode and then multiple relatively flat optical modes, consistent with weak inter-site exchange and strongly localized intra-cell excitations at higher energy eigenvalues. The flat bands are the spin precessions localized to their own unit-cell and hence do not propagate.[60] Moreover, the scattering intensity of the optical modes interfere destructively at the center of the Brillouin zone and hence seem to be vanishing. Mn, Co and Fe display the strongest effective exchanges, with high acoustic bandwidths and magnon frequencies extending up to 15 THz. Their spectra combine dispersive acoustic modes which are favorable for long lifetime with well-

separated optical groups with the caveat that only the lowest modes are propagating. The bands in Ni collapse into nearly dispersionless bands tightly clustered at extremely low energies, indicating very weak exchange and highly localized spin excitations.

From an applications perspective, Mn- and Co-functionalized strips are promising where higher-frequency magnonic response or long-range magnon transport is required; Cr is more suited to low-frequency, localized resonant magnonic elements. The existence of acoustic-optical magnonic bandgaps between acoustic mode ($n = 0$) and first optical mode ($n = 1$) of the Fe and Cr based strips has the advantage of being able to use the acoustic magnons which possess longer lifetimes along with optical modes to filter or select frequencies. In the optical region, significant bandgaps exist between first and second optical modes of Cr, Mn, Co which may prove to be quite useful. However, this is not the case for Fe-based system. Since the third optical mode for Mn is dispersive, the bandgap between second and third optical mode is also important for Mn while not so for the other adatoms.

3.3. Group velocities

The group velocity was calculated to obtain the propagation velocity of spin waves in the strip for each adatom. It is the gradient of the eigenenergy of each mode with respect to the wavevector.

$$V_g = \frac{dE}{dq}, \tag{8}$$

where $E(q)$ is the magnon energy at a given wave vector q. The resulting velocities for all transition-metal (TM) adatoms are presented in Fig. 5.

The spin waves propagate symmetrically in both directions around the Γ-point, due to the symmetric nature of the magnon dispersion relations. The group velocity goes to 0 at the Γ-point, which also includes thermal excitations, and at the Brillouin-zone edges, reaching its maximum at intermediate wave vectors ($q \approx 0.3$–0.5 Å^{-1}), where the slope of the dispersion curve is steepest.

From Fig. 5, it can be seen that Mn- and Co-decorated strips exhibit the largest group velocities as these have the highest exchange interaction energies and therefore greater stiffness. The acoustic branch in these systems reaches up to 5.2 km s^{-1} for Mn and 5.0 km s^{-1} for Co. Their first optical branches also sustain high propagation speeds exceeding 3 km s^{-1}. Both these systems also display velocities >2 km s^{-1} for modes $n = 3$ and $n = 4$, suggesting that multiple channels can contribute to magnon transport. The coexistence of several high-velocity modes can be understood from high stiffness modes seen in the dispersion relation in Fig. 4b and d. These along with suitable bandgaps are advantageous for coherent spin wave transmission and potential magnonic device operation.

Meanwhile, the Fe-decorated strip shows moderate group velocities of approximately 2 km s^{-1} for the acoustic and first optical modes. Although its highest magnon mode lying at 10 THz is comparable to that of Mn and Co; the contribution from antiferromagnetic exchange interaction in Fe reduces the effective stiffness of the dispersion of Fe-decorated strip and therefore lowers the group velocity leading to slower spin wave propagation. The Cr- and Ni-based systems exhibit the lowest velocities; in particular, Ni shows nearly flat modes across the Brillouin zone, as it has weak exchange coupling and diminished spin stiffness.

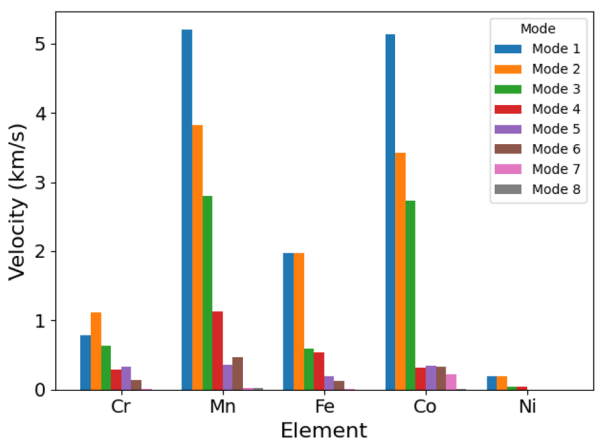

Fig. 5 The highest group velocity available for propagation in each mode for each adatom decorated holey graphyne strip.

3.4. Tuning dispersion using a magnetic field

We analyze the evolution of the three low-lying magnon modes and the associated bandgaps under an external magnetic field applied perpendicular to the direction of propagation from 0 to 1 T. The applied field, B, introduces a Zeeman term, $g\mu_B B M_{eff}(q)$, which couples with the effective magnetization, M_{eff}, at each wavevector q. In our case with only exchange interactions, the effective magnetization does not change significantly with q as shown in Fig. 6.

The introduction of the Zeeman term into the magnon Hamiltonian shifts the magnon energies of the acoustic mode upward, which corresponds to a finite energy requirement to excite the mode even at the Γ point. Meanwhile, the effect on other modes depends on the relative magnetization and amplitude of the mode with respect to the field direction. As each mode has a different effective magnetization given that there are 8 interacting sublattices, the effective magnetization and hence the shifts due to magnetic field are different for different modes which leads to opening or closing of bandgaps.

As seen in Fig. 6c, all three modes of chromium respond uniformly to the external field, leaving the bandgaps between mode 1 and mode 2 at 0.13 and 0.47 THz between mode 2 and 3 effectively unchanged between 0 and 1 T. In iron (Fe), the gap between mode 2 and mode 3 decreases with increasing field and almost closes around $B \approx 1$ T. This happens as mode 3 decreases when magnetic field is increased. In case of Mn, the bandgap between acoustic and optical mode doesn't exist, and the trend is for the first optical mode to shift downward as can be seen in Fig. 6b. The same shift however, creates about 11%

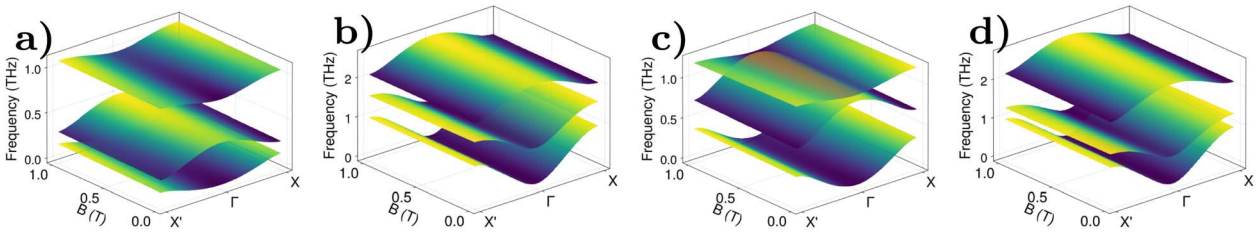

Fig. 6 Evolution of the first three modes of the dispersion relation when the magnetic field is applied along the z-axis for the $C_{40}TM_8$ systems with adatoms: (a) Cr, (b) Mn, (c) Fe, (d) Co. The colormap shows the gradient from highest (dark blue) to lowest (yellow).

change in the bandgap between mode 2 (first optical mode) and mode 3 reaching 0.54 THz. The Co-adatom system mimics Mn but the change is only about 6% as the first optical mode couples weakly with external field.

4. Conclusion

We have investigated the structural and magnetic properties of transition metal (TM = V, Cr, Mn, Fe, Co, Ni) adatoms on a holey graphyne strip using DFT and linear spin-wave theory. The optimized structures are thermally stable at ambient conditions. Magnetic moments show a volcano trend across the series of transition metals, peaking at Mn due to the availability of more unpaired electrons after Dewar interactions. Exchange interactions indicate ferrimagnetic ordering with strong ferromagnetic couplings, while V exhibits negligible magnetism.

Magnon dispersions show eight modes per unit cell with a gapless acoustic branch. Mn and Co adatoms have several dispersive optical modes with high group velocities, making them the most promising for spin wave applications. Bandgaps between acoustic and first optical modes, as well as between higher optical modes, can be tuned with an external magnetic field, enabling selective frequency control. Hence, Mn- and Co-decorated graphyne strips emerge as promising platforms for high-speed, tunable spin wave devices requiring experimental verification. Fe and Cr offer moderate performance, whereas Ni shows limited propagation due to flatter bands and lower velocities.

Conflicts of interest

There are no conflicts to declare.

Data availability

The data supporting the findings of this study are available from the corresponding author upon reasonable request.

Supplementary information (SI): figures and derivations that are not presented in the manuscript. See DOI: https://doi.org/10.1039/d5ra09647b.

Acknowledgements

One of the authors, Debashis Bandyopadhyay, would like to acknowledge the Science and Engineering Research Board (SERB), Govt. of India, India, for using the research support provided under the sanction order number CRG/2022/003249 for this work.

References

1 R. Schaller, *EEE Workshop Comput. Vis. Beyond Visible Spectr. Methods Appl.*, 1997, **34**, 52.
2 A. V. Chumak, A. A. Serga and B. Hillebrands, *Nat. Commun.*, 2014, **5**, 4700.
3 A. V. Chumak, V. I. Vasyuchka, A. A. Serga and B. Hillebrands, *Nat. Phys.*, 2015, **11**, 453.
4 S. Neusser and D. Grundler, *Adv. Mater.*, 2009, **21**, 2927.
5 A. V. Chumak, P. Kabos, M. Wu, C. Abert, C. Adelmann, A. O. Adeyeye, J. Åkerman, F. G. Aliev, A. Anane, A. Awad and C. H. Back, *IEEE Trans. Magn.*, 2022, **58**, 1.
6 Y. V. Gulyaev, S. A. Nikitov, L. V. Zhivotovskii, A. A. Klimov, P. Tailhades, L. Presmanes, C. Bonningue, C. S. Tsai, S. L. Vysotskii and Y. A. Filimonov, *J. Exp. Theor. Phys. Lett.*, 2003, **77**, 567.
7 M. Krawczyk and D. Grundler, *J. Phys.: Condens. Matter*, 2014, **26**, 123202.
8 T. Langner, D. A. Bozhko, S. A. Bunyaev, G. N. Kakazei, A. V. Chumak, A. A. Serga, B. Hillebrands and V. I. Vasyuchka, *J. Phys. D: Appl. Phys.*, 2018, **51**, 344002.
9 Z. K. Wang, V. L. Zhang, H. S. Lim, S. C. Ng, M. H. Kuok, S. Jain and A. O. Adeyeye, *Appl. Phys. Lett.*, 2009, **94**, 083112.
10 A. V. Sadovnikov, A. A. Grachev, S. E. Sheshukova, Y. P. Sharaevskii, A. A. Serdobintsev, D. M. Mitin and S. A. Nikitov, *Phys. Rev. Lett.*, 2018, **120**, 257203.
11 X. S. Wang, Y. Su and X. R. Wang, *Phys. Rev. B*, 2017, **95**, 014435.
12 P. Che, R. Ciola, M. Garst, V. Kravchuk, P. R. Baral, A. Magrez, H. Berger, T. Schönenberger, H. M. Rønnow and D. Grundler, *Commun. Mater.*, 2025, **6**, 139.
13 M. Madami, S. Bonetti, G. Consolo, S. Tacchi, G. Carlotti, G. Gubbiotti, F. B. Mancoff, M. A. Yar and J. Åkerman, *Nat. Nanotechnol.*, 2011, **6**, 635.
14 V. E. Demidov, S. Urazhdin, R. Liu, B. Divinskiy, A. Telegin and S. O. Demokritov, *Nat. Commun.*, 2016, **7**, 10446.
15 S. Wintz, V. Tiberkevich, M. Weigand, J. Raabe, J. Lindner, A. Erbe, A. Slavin and J. Fassbender, *Nat. Nanotechnol.*, 2016, **11**, 948.
16 H.-B. Li and Z.-G. Shao, *Phys. Rev. B*, 2025, **111**, 214420.
17 K. Zakeri, *J. Phys. Condens. Matter*, 2020, **32**, 363001.

18 X. Yao, Z. Jin, Z. Wang, Z. Zeng and P. Yan, *Phys. Rev. B*, 2023, **108**, 134427.
19 H. J. Qin, K. Zakeri, A. Ernst, L. M. Sandratskii, P. Buczek, A. Marmodoro, T.-H. Chuang, Y. Zhang and J. Kirschner, *Nat. Commun.*, 2015, **6**, 6126.
20 K. Zakeri, *Physica C*, 2018, **549**, 164.
21 P. Li, X. Li, J. Feng, J. Ni, Z.-X. Guo and H. Xiang, *Phys. Rev. B*, 2024, **109**, 214418.
22 K. Zakeri and A. Ernst, *Nano Lett.*, 2024, **24**, 9528.
23 A. T. Costa, R. B. Muniz and D. L. Mills, *Phys. Rev. B Condens. Matter*, 2004, **70**, 054406.
24 H. J. Qin, S. Tsurkan, A. Ernst and K. Zakeri, *Phys. Rev. Lett.*, 2019, **123**, 257202.
25 L. Bergqvist, A. Taroni, A. Bergman, C. Etz and O. Eriksson, *Phys. Rev. B Condens. Matter*, 2013, **87**, 144401.
26 A. B. Ustinov, A. V. Drozdovskii and B. A. Kalinikos, *Appl. Phys. Lett.*, 2010, **96**, 142513.
27 M. Krawczyk and H. Puszkarski, *Phys. Rev. B Condens. Matter*, 2008, **77**, 054437.
28 K. Di, V. L. Zhang, M. H. Kuok, H. S. Lim, S. C. Ng, K. Narayanapillai and H. Yang, *Phys. Rev. B Condens. Matter*, 2014, **90**, 060405.
29 S. Klingler, P. Pirro, T. Brächer, B. Leven, B. Hillebrands and A. V. Chumak, *Appl. Phys. Lett.*, 2014, **105**, 152410.
30 T. Song, Z. Fei, M. Yankowitz, Z. Lin, Q. Jiang, K. Hwangbo, Q. Zhang, B. Sun, T. Taniguchi, K. Watanabe, M. A. McGuire, D. Graf, T. Cao, J.-H. Chu, D. H. Cobden, C. R. Dean, D. Xiao and X. Xu, *Nat. Mater.*, 2019, **18**, 1298.
31 T. Li, S. Jiang, N. Sivadas, Z. Wang, Y. Xu, D. Weber, J. E. Goldberger, K. Watanabe, T. Taniguchi, C. J. Fennie, K. Fai Mak and J. Shan, *Nat. Mater.*, 2019, **18**, 1303.
32 S. Kim, A. Ruiz Puigdollers, P. Gamallo, F. Viñes and J. Y. Lee, *Carbon*, 2017, **120**, 63.
33 F. S. Ma, H. S. Lim, V. L. Zhang, S. C. Ng and M. H. Kuok, *Nanoscale Res. Lett.*, 2012, **7**, 498.
34 N. Kanazawa, T. Goto and M. Inoue, *J. Appl. Phys.*, 2014, **116**, 083903.
35 K.-S. Lee, D.-S. Han and S.-K. Kim, *Phys. Rev. Lett.*, 2009, **102**, 127202.
36 B. Huang, G. Clark, E. Navarro-Moratalla, D. R. Klein, R. Cheng, K. L. Seyler, D. Zhong, E. Schmidgall, M. A. McGuire, D. H. Cobden, W. Yao, D. Xiao, P. Jarillo-Herrero and X. Xu, *Nature*, 2017, **546**, 270.
37 D. Lujan, J. Choe, M. Rodriguez-Vega, Z. Ye, A. Leonardo, T. N. Nunley, L.-J. Chang, S.-F. Lee, J. Yan, G. A. Fiete, R. He and X. Li, *Nat. Commun.*, 2022, **13**, 2527.
38 D. L. Esteras, A. Rybakov, A. M. Ruiz and J. J. Baldoví, *Nano Lett.*, 2022, **22**, 8771.
39 L. Lu, Q. Wang, H. Duan, K. Zhu, T. Hu, Y. Ma, S. Shen, Y. Niu, J. Liu, J. Wang, S. A. Ekahana, J. Dreiser, Y. Soh, W. Yan, G. Wang, Y. Xiong, N. Hao, Y. Lu and M. Tian, *Nano Lett.*, 2024, **24**, 5984.
40 C. Wu, H. Sun, P. Dong, Y.-Z. Wu and P. Li, *Adv. Funct. Mater.*, 2025, **35**, 2501506), _eprint: https://doi.org/10.1002/adfm.202501506.
41 S. Jenkins, L. Rózsa, U. Atxitia, R. F. L. Evans, K. S. Novoselov and E. J. G. Santos, *Nat. Commun.*, 2022, **13**, 6917.
42 S. Bhattacharyya, *Carbon Superstructures: from Quantum Transport to Quantum Computation*, CRC Press, 2024.
43 C. P. Bhat and D. Bandyopadhyay, *Int. J. Hydrogen Energy*, 2024, **79**, 377.
44 C. P. Bhat and D. Bandyopadhyay, *Int. J. Hydrogen Energy*, 2025, **137**, 750.
45 C. P. Bhat, B. Bandyopadhyay and D. Bandyopadhyay, *Int. J. Hydrogen Energy*, 2025, **148**, 150044.
46 J. Pan, S. Du, Y. Zhang, L. Pan, Y. Zhang, H.-J. Gao and S. T. Pantelides, *Phys. Rev. B*, 2015, **92**, 205429.
47 X. Liu1, S. M. Cho, S. Lin, E. Yun, E. H. Baek, Z. Chen, D. H. Ryu, and H. Lee, *Direct Band Gap Semiconducting Holey Graphyne: Structure, Synthesis and Potential Applications*, 2019.
48 M. Sajjad, K. Badawy, J. A. Larsson, R. Umer and N. Singh, *Carbon*, 2023, **214**, 118340.
49 Y.-C. Jiang, T. Kariyado and X. Hu, *Nanotechnology*, 2024, **35**, 195201.
50 A. A. Mostofi, J. R. Yates, Y.-S. Lee, I. Souza, D. Vanderbilt and N. Marzari, *Comput. Phys. Commun.*, 2008, **178**, 685.
51 X. He, N. Helbig, M. J. Verstraete and E. Bousquet, *Comput. Phys. Commun.*, 2021, **264**, 107938.
52 D. Dahlbom, H. Zhang, C. Miles, S. Quinn, A. Niraula, B. Thipe, M. Wilson, S. Matin, H. Mankad, S. Hahn, D. Pajerowski, S. Johnston, Z. Wang, H. Lane, Y. W. Li, X. Bai, M. Mourigal, C. D. Batista, and K. Barros, *A Julia Package for Spin Dynamics*, 2025.
53 G. Kresse and J. Hafner, *J. Phys.: Condens. Matter*, 1994, **6**, 8245.
54 G. Kresse and J. Furthmüller, *Comput. Mater. Sci.*, 1996, **6**, 15.
55 G. Kresse and J. Furthmüller, *Phys. Rev. B Condens. Matter*, 1996, **54**, 11169.
56 R. Tesch and P. M. Kowalski, *Phys. Rev. B Condens. Matter*, 2022, **105**, 195153.
57 M. I. Katsnelson and A. I. Lichtenstein, *Phys. Rev. B Condens. Matter*, 2000, **61**, 8906.
58 S. Toth and B. Lake, *J. Phys.: Condens. Matter*, 2015, **27**, 166002.
59 C. Kittel and P. McEuen, *Introduction to Solid State Physics* (John Wiley & Sons, 2018).
60 S. X. M. Riberolles, T. J. Slade, T. Han, B. Li, D. L. Abernathy, P. C. Canfield, B. G. Ueland, P. P. Orth, L. Ke and R. J. McQueeney, *Nat. Commun.*, 2024, **15**, 1592.